Layer number dependent spin Hall effects in transition metal monocarbides M_2C (M = V, Nb, Ta)

Xi Zuo,[1] Yulin Feng,[1] Na Liu,[1] Bing Huang,[2,3] Meifeng Liu,[1] Desheng Liu,[4,*] and Bin Cui[4,†]

[1]*College of Physics and Electronic Science, Hubei Key Laboratory of Photoelectric Conversion Materials and Devices, Hubei Normal University, Huangshi 435002, China*

[2]*Beijing Computational Science Research Center, Beijing 100193, China*

[3]*Beijing Normal University, Beijing 100875, China*

[4]*School of Physics, National Demonstration Center for Experimental Physics Education, Shandong University, Jinan 250100, China*

(Received 16 October 2022; revised 6 September 2023; accepted 11 October 2023; published 15 November 2023)

The recent discovery of strong spin Hall effects (SHEs) in two-dimensional layered topological semimetals has attracted intensive attention due to their exotic electronic properties and potential applications in spintronic devices. In this paper, we systematically study the topological properties and intrinsic SHEs of layered transition metal carbides M_2C (M = V, Nb, Ta). The results show that d bands crossing near the Fermi level (E_F) induce multiple nodal lines (NLs) and nodal points (NPs) in bulk and few-layered M_2C, respectively. The inclusion of spin-orbit coupling breaks the degeneracy of NLs and NPs, contributing to large spin Hall conductivity (SHC) up to ∼1100 and ∼ 200 $(\hbar/e)(\Omega\,\mathrm{cm})^{-1}$ for bulk and monolayer Ta_2C, respectively. Remarkably, we find that the magnitude of SHC exhibits a significant enhancement by increasing the layer thickness. For eight-layer Ta_2C, the maximum value of SHC can reach up to ∼ 600 $(\hbar/e)(\Omega\,\mathrm{cm})^{-1}$, comparable to many reported three-dimensional topological materials. Analysis of spin Berry curvature reveals that the large SHC originates from layer number dependent nodal-point structure near the E_F, around where the repeated crossover between the valence and conduction bands creates large numbers of NPs in the Γ-K and Γ-M routes. Our findings not only provide a platform for experimental research of low-dimensional SHE, but also suggest an effective way of realizing giant SHE by controlling layer thickness.

DOI: 10.1103/PhysRevB.108.195129

I. INTRODUCTION

The Spin Hall effect (SHE), a relativistic phenomenon in which electrical currents can generate transverse spin currents in the absence of magnetic field, has become an important topic in recent years [1–11]. Two key factors, intrinsic spin Hall conductivity (SHC) and spin Hall angle (SHA), influence the performance of SHE-based devices. The intrinsic SHC can be accurately calculated by integrating the spin Berry curvature (SBC) of the occupied bands in the Brillouin zone (BZ) [12]. The SHA of a SHE system is the ratio of the SHC to the charge conductivity (G_C), which represents the charge to spin interconversion efficiency at room temperature [13]. Therefore, exploring SHE systems with large SHC and SHA is one of the main goals in this field.

With the rapid development of topological matters, strong SHE is observed in topological systems such as topological insulators (TIs) and topological semimetals (TSMs) [14–16]. Due to their spin momentum locked surface states, TIs are considered to be ideal systems for generating pure spin currents. However, various experiments show that the SHA of the Bi_2Se_3 family can vary from 0.01 to 425 due to the bulk doping problem induced by the hybridization between surface and bulk states [14,17,18]. Recently, increasing attention has been focused on the intrinsic SHE in TSMs. For example, nodal-point semimetals HfCuGeAs [9], ZrSiTe [19], and TaAs [20] have been predicted to host large intrinsic SHC exceeding 500 $(\hbar/e)(\Omega\,\mathrm{cm})^{-1}$ due to large SBC around the spin-orbit coupling (SOC) induced small-gapped Dirac or Weyl nodal points. On the other hand, large intrinsic SHEs have also been reported in nodal-line semimetals. Different from nodal-point semimetals, the gapped nodal lines can induce many band anticrossing points distributed with large and continuous SBC in the entire BZ, contributing to a remarkable SHC [21]. It is predicted that nodal-line TSMs (NLSMs) such as W_3Ta [22], Ta_3Bi [23], and InBi [24] exhibit giant SHC exceeding 1000 $(\hbar/e)(\Omega\,\mathrm{cm})^{-1}$ at the Fermi level (E_F). To realize large intrinsic SHC and SHA as well as to design ideal devices for spin-charge current conversion, it is important to explore new TSMs and study the interplay between the SHC and the band topology.

Recently, the two-dimensional (2D) transition metal dichalcogenides (TMDs) family has been reported to exhibit large SHE due to their tunable SOC, G_C, and band topology [25–27]. For example, the Weyl semimetals $MoTe_2$ and WTe_2 are reported to have a large SHA of 0.32 [28] and 0.17 [29], respectively. Spin-orbit torque in few-layered Dirac semimetal $PtTe_2$ [30] reveals that the SHC exhibits a monotonical increment with a maximum value of about 1000 $(\hbar/e)(\Omega\,\mathrm{cm})^{-1}$ as the layer thickness increases from 3 to 20 nm. Correspondingly, first-principles calculations on bilayer $PtSe_2$ [31] and trilayer $MoTe_2$ [28] reveal that its intrinsic SHC is about 27 and 200 $(\hbar/e)(\Omega\,\mathrm{cm})^{-1}$ at the E_F, respectively. This raises the question of whether we can find large intrinsic SHC in

*liuds@sdu.edu.cn
†cuibin@sdu.edu.cn

layered 2D materials comparable to familiar heavy metals or there-dimensional (3D) topological materials. On the other hand, the influence of layer thickness on the SHE in 2D materials still calls for further theoretical investigation.

In this paper, we systematically investigate electronic structures and intrinsic SHE in 2D layered transition metal carbides M_2C (M = V, Nb, Ta, known as MXenes), which exhibit a fascinating combination of properties such as controllable minimum layer thickness, large electric conductivities, and rich electronic structures, and can be easily synthesized in the laboratory [32–37]. Both bulk and monolayer M_2C exhibit large SHC owing to strong SOC and contributions of multiple nodal lines or nodal points in the band structures. Taking Ta_2C as an example, we observe a significant enhancement of SHC by varying the thickness from one layer (1L) to eight layers (8L), which originates from the layer number dependent nodal-point structures near the E_F. The rest of this article is organized as follows. In Sec. III A, we first give the description of crystal structures for bulk and monolayer M_2C. In Sec. III B, we then report the band structures, SHC, and SHA for bulk M_2C. In Sec. III C, we study the SHE of few-layered M_2C by varying the layer number from 1L up to 8L. To understand the origin of layer number dependent SHC, we also give the electronic band structures, nodal-point structures, and k-resolved SBC at E_F. Finally, the conclusion drawn from this work is summarized in Sec. IV.

II. THEORY AND COMPUTATIONAL DETAILS

First-principles calculations are carried out by using the density-functional theory (DFT) as implemented in the QUANTUM ESPRESSO package [38]. Projector-augmented wave (PAW) [39] and the generalized gradient approximation (GGA) with the Perdew-Burke-Ernzerhof (PBE) functional [40] are used to describe the potential of core electrons and the exchange-correlation interaction between the valence electrons, respectively. The valence configurations of V, Nb, Ta, and C atoms are $3s^2 4s^2 3p^6 3d^3$, $4s^2 5s^2 4p^6 4d^3$, $5s^2 6s^2 5p^6 5d^3 4f^{14}$, and $2s^2 2p^2$, respectively. To explore the SHC and the SHA, the tight-binding Hamiltonians are constructed with the maximally localized Wannier functions [41,42] for the outermost s and d orbitals of V, Nb, and Ta atoms and the outermost p orbitals of C atoms generated by the first-principles calculations. The Wannier-fitted band structures are shown in Figs. S1 and S2 in the Supplemental Material (SM) [43].

Based on the tight-binding model constructed with WANNIER90, the nodal lines and points are calculated using the WANNIERTOOLS software package [44]. To get the accurate nodal lines in the whole Brillouin zone (BZ), we first symmetrize the tight-binding Hamiltonian according to the crystal symmetries and then find all the nodal points in the BZ.

Based on the Wannier-interpolation approach, we calculate SHC in the clean limit using the Kubo formula [13]:

$$\sigma_{ij}^{k} = -\frac{e^2}{\hbar}\frac{1}{VN_k}\sum_{n}\sum_{\boldsymbol{k}} f_{n\boldsymbol{k}}\Omega_{n,ij}^{k}(\boldsymbol{k}), \tag{1}$$

$$\Omega_{n,ij}^{k}(\boldsymbol{k}) = \hbar\sum_{m\neq n}\frac{-2\mathrm{Im}\left[\langle n\boldsymbol{k}|\hat{j}_i^k|m\boldsymbol{k}\rangle\langle m\boldsymbol{k}|\hat{v}_j|n\boldsymbol{k}\rangle\right]}{(E_{nk}-E_{mk})^2}, \tag{2}$$

Here, $\hat{j}_i^k = \frac{1}{2}\{\hat{s}_k,\ \hat{v}_i\}$ is the spin current operator, with the spin operator $\hat{s}_k = \frac{\hbar}{2}\hat{\sigma}_k$, the velocity operator $\hat{v}_i = \frac{1}{\hbar}\frac{\partial H(\boldsymbol{k})}{\partial k_i}$, and $i,\ j,\ k = x,\ y,\ z$. $|n\boldsymbol{k}\rangle$ is the eigenvector of the Hamiltonian H corresponding to eigenvalue $E_{n\boldsymbol{k}}$. $f_{n\boldsymbol{k}}$ is the Fermi-Dirac distribution for the nth band. V is the primitive cell volume, and N_k is the number of k points sampling in the BZ. The unit of σ_{ij}^k is $(\hbar/e)(\Omega\,\mathrm{cm})^{-1}$. $\Omega_{n,ij}^k$ is referred to as the spin Berry curvature (SBC) in units of Å. For bulk M_2C, a $100\times100\times100$ Wannier-interpolation k mesh with a $4\times4\times4$ adaptive refinement k mesh is used for the integral of the SHC. For SHC calculations of few-layered M_2C, the cell volume V in the denominator of expression (1) corresponds to the primitive cell used in the DFT calculations which includes the vacuum thickness.

The SHA is defined as the ratio of the SHC over the G_C, which characterizes the efficiency of converting the charge current to spin current. The SHA is evaluated according to

$$\theta_{\mathrm{SH}} = \frac{2e}{\hbar}\frac{\sigma_{xy}^{z}}{\sigma_{xx}}, \tag{3}$$

where σ_{xx} is the longitudinal G_C and σ_{xy}^z is the transverse SHC. The longitudinal σ_{xx} is calculated by using the Boltzmann transport equations within the constant relaxation time approximation as follows [45]:

$$[\sigma]_{ij}(\mu,\ T) = e^2\int_{-\infty}^{+\infty}\left[-\frac{\partial f(\varepsilon,\mu,T)}{\partial(\varepsilon)}\right]\Sigma_{ij}(\varepsilon), \tag{4}$$

$$\Sigma_{ij}(\varepsilon) = \frac{1}{V}\sum_{n,k}\nu_i(n,\ \boldsymbol{k})\nu_j(n,\ \boldsymbol{k})\tau(n,\ \boldsymbol{k})\delta(\varepsilon - E_{n,k}), \tag{5}$$

where μ is the chemical potential, $f(\varepsilon,\mu,T)$ is the Fermi-Dirac distribution function $f(\varepsilon,\mu,T) = \frac{1}{e^{(\varepsilon-\mu)/k_{\mathrm{B}}T}+1}$, $\Sigma_{ij}(\varepsilon)$ is the transport distribution function tensor, $E_{n,k}$ is the energy of the nth band at $\mathbf{k}$, $\nu_i(n,\ \boldsymbol{k})$ is the ith component of the band velocity at $(n,\ \boldsymbol{k})$, δ is the Dirac's delta function, V is the total volume of the system, and $\tau_{n,k}$ is the relaxation time depending on band and wave vector, which describes the collision term in the Boltzmann equation. In the calculation, we assume that the lifetime $\tau_{n,k}$ is independent of both n and k and choose the value $\tau = \tau_{n,k}$ by fitting the experimental electric conductivities at a given temperature. For monolayer M_2C (M = V, Nb, Ta), due to lack of experimental G_C values, we directly obtain the electron relaxation times by evaluating the electron-phonon coupling using the EPW code [46] (see calculation details in Fig. S3 in the SM [43]).

III. RESULTS

A. Crystal structure

As shown in Fig. 1(a), the bulk M_2C (M = V, Nb, Ta) crystallizes in a trigonal crystal structure with the space group $P\bar{3}m1$ (164). The C atom is located at the corner sites of the unit cell, while two M atoms are located at equivalent sites with the Wyckoff position of $2d$ (1/3, 2/3, 1/4). Each C atom is bonded to six equivalent M atoms to form an edge-sharing octahedral, and each M atom is bonded in a distorted T-shaped geometry to three equivalent C atoms. The optimized lattice parameters for bulk and monolayer M_2C are summarized in Table I; they agree well with previous experimental and

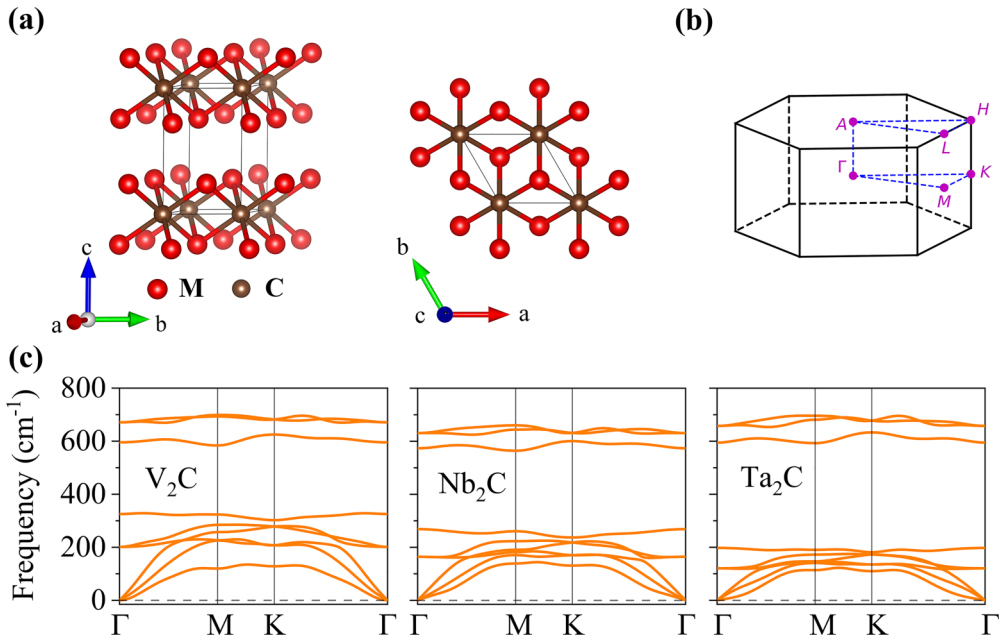

FIG. 1. (a) Side and top views of crystal structures of bulk M_2C (M = V, Nb, Ta). (b) Brillouin zone (BZ) of a primitive cell of M_2C. (c) Calculated phonon dispersions along high-symmetry lines for monolayer M_2C (M = V, Nb, Ta).

theoretical values [47,48]. The BZ is shown in Fig. 1(b). The phonon spectra of energetically stable crystal structures for monolayer M_2C (M = V, Nb, Ta) are calculated and shown in Fig. 1(c). Obviously, the phonon spectra contain no imaginary frequency, indicating that monolayer M_2C (M = V, Nb, Ta) are dynamically stable [36]. For few-layered Ta_2C, we first cleave the bulk phase and add at least 20 vacuum thicknesses to avoid interactions between neighboring unit cells. The corresponding lattice parameters are shown in Table S1 in the Supplemental Material (SM) [43].

B. Electronic band structures and SHE in bulk M_2C

Based on the optimized structures, the calculated band structures in the absence of SOC for bulk Ta_2C are shown in Fig. 2(a), and those of other compounds are displayed in Fig. S4 in the SM [43], respectively. The orbital character analysis shows that the 5*d* orbitals of Ta dominate the bands near the E_F. Interestingly, several bands cross each other and form the nodal points P1 and P2 and nodal line L1. Here, we label the three bands that contribute to the nodal lines as $EB_{k=1,2,3}$ sorted by energy values. To clearly distinguish these bands, the top of the valence band, namely, EB_2, has been colored red. It is observed that the EB_2 and EB_3 bands are degenerate along the Γ-*A* route, and induce the nodal line L1. On the other hand, P1 is formed by the band crossing of EB_1 and EB_2 along *K*-Γ, while P2 is formed by the band crossing of EB_2 and EB_3 along the *L*-*H* routes. The multiple band degeneracies around E_F imply the nodal-line structure in Ta_2C. To confirm our physical intuition, we perform a systematic

TABLE I. The optimized lattice parameters for bulk and monolayer M_2C (M = V, Nb, Ta).

	Bulk				Monolayer	
M_2C	a (Å)	Ref.	c (Å)	Ref.	a (Å)	Ref.
V_2C	2.892	2.904[a]	4.521	4.579[a]	2.886	2.883[b]
Nb_2C	3.140	3.120[c]	4.984	4.957[c]	3.124	3.117[b]
Ta_2C	3.122	3.103[a]	4.953	4.937[a]	3.080	3.084[b]

[a]X-ray diffraction experiment data [47].
[b]*Ab initio* calculation [35].
[c]Experiment data [48].

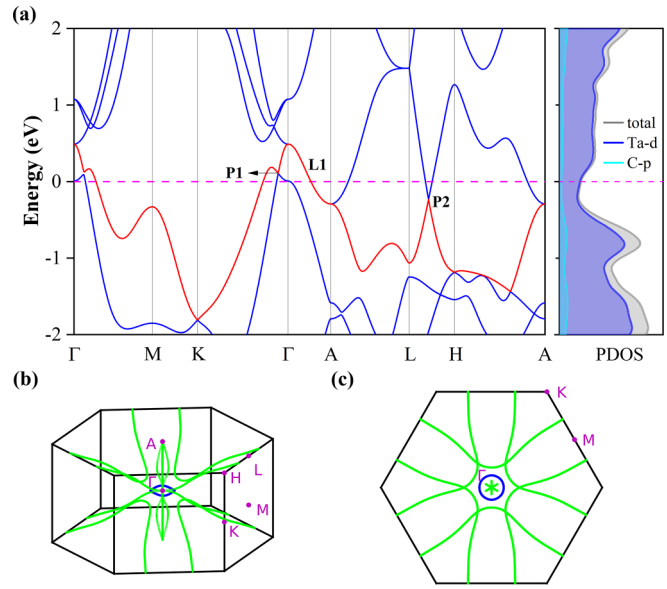

FIG. 2. (a) Band structure and projected density of states of bulk Ta_2C without SOC. P1, P2, and L1 represent the two nodal points and nodal line in the band structure, respectively. The highest valence band is shown in red. (b) Nodal lines in the first BZ. (c) Top view of the nodal lines. The E_F is set to zero in (a).

TABLE II. The irreducible representations (Irreps) of the electronic bands of the little group at different high-symmetry points in the first BZ of Ta_2C without SOC. The Irreps corresponding to the higher-energy bands are placed at the top of the table, which are written in the BCS convention. The numbers in the parentheses indicate the dimensions of the Irreps and the degree of degeneracy of the bands at the corresponding high-symmetry points. The superscript +/– means the parity.

M	K	Γ	A	L	H
M_2^- (1)	K_3 (2)	Γ_3^+ (2)	A_3^+ (2)	L_2^- (1)	H_1 (1)
M_2^- (1)	K_3 (2)	Γ_1^+ (1)	A_2^- (1)	L_1^+ (1)	H_3 (2)
M_1^+ (1)				L_2^- (1)	

nodal-line search in the first BZ. Here, we first identify all the k points with zero energy gap between the EB_2 and EB_3 bands and plot them with green lines in Figs. 2(b) and 2(c). A similar treatment is used in the nodal-line search between the EB_1 and EB_2 bands, which is shown with blue lines. There are 11 nodal lines near the E_F that can be classified into three classes: class I, the closed nodal ring around the Γ point; class II, three curved nodal lines and one straight nodal line crossing the Γ point around the Γ-A route; and class III, six paraboliclike nodal lines connecting the horizontal edges of the BZ. We also show each class of nodal line in the first BZ in Fig. S5 in the SM [43].

Here, based on symmetry analysis, we reveal the symmetry protection mechanism of the nodal points and lines formed by EB_1-EB_3. For bulk M_2C (M = V, Nb, Ta), the generators of the space group $P\bar{3}m1$ (164) are C_{3z}, inversion symmetry ($\mathcal{P}$), and twofold rotational symmetry $C_{2(110)}$. Meanwhile, we also have time-reversal symmetry ($\mathcal{T}$) in this system. To figure out the symmetry protection of nodal lines in this system without SOC, we have calculated the irreducible representations (Irreps) at different high-symmetry points, which are shown in Table II. It is noted the results are written in the Bilbao Crystallographic Server (BCS) convention.

For nodal line L1 along Γ-A, the high-symmetry line is invariant under threefold rotation symmetry C_{3z} and joint symmetry $\mathcal{PT}$, which belongs to the C_{3v} point group symmetry. From Table II, the Irreps at Γ and A are Γ_3^+ (2) and A_3^+ (2), respectively. By checking the compatibility relations along Γ-A, we find the Irreps for an arbitrary point k_0 on the Γ-A is Δ_3 (2). The dimension of this Irrep is 2 and the corresponding matrix form of C_{3z} is $e^{i\sigma_z 2\pi/3}$; here σ_z is the Pauli matrix. For a Bloch state $|\phi^{\pm}\rangle$ with the eigenvalue $e^{\pm i2\pi/3}$ of C_{3z} at k_0, we have

$$C_{3z}\mathcal{PT}|\phi^{\pm}\rangle = \mathcal{PT}C_{3z}|\phi^{\pm}\rangle = e^{\pm i2\pi/3}\mathcal{PT}|\phi^{\pm}\rangle, \qquad (6)$$

where the commutation relation $[C_{3z}, \mathcal{PT}] = 0$ is adopted. Thus, the two states $|\phi^{\pm}\rangle$ and $\mathcal{PT}|\phi^{\pm}\rangle$ must be degenerate at k_0, indicating that L1 is protected by C_{3z} associated with $\mathcal{PT}$ symmetry. For nodal point P1 along K-Γ, the little group of an arbitrary point k_1 is the C_2 point group and the maintained symmetries are $\mathcal{PT}$ and twofold rotational symmetry $C_{2(110)}$. The little group Irreps at k_1 are Λ_1 (1) and Λ_2 (1) with opposite eigenvalues of $C_{2(110)}$. Similar analysis reveals that P2 along the L-H route is also protected by rotational symmetry $C_{2(010)}$ associated with $\mathcal{PT}$ symmetry.

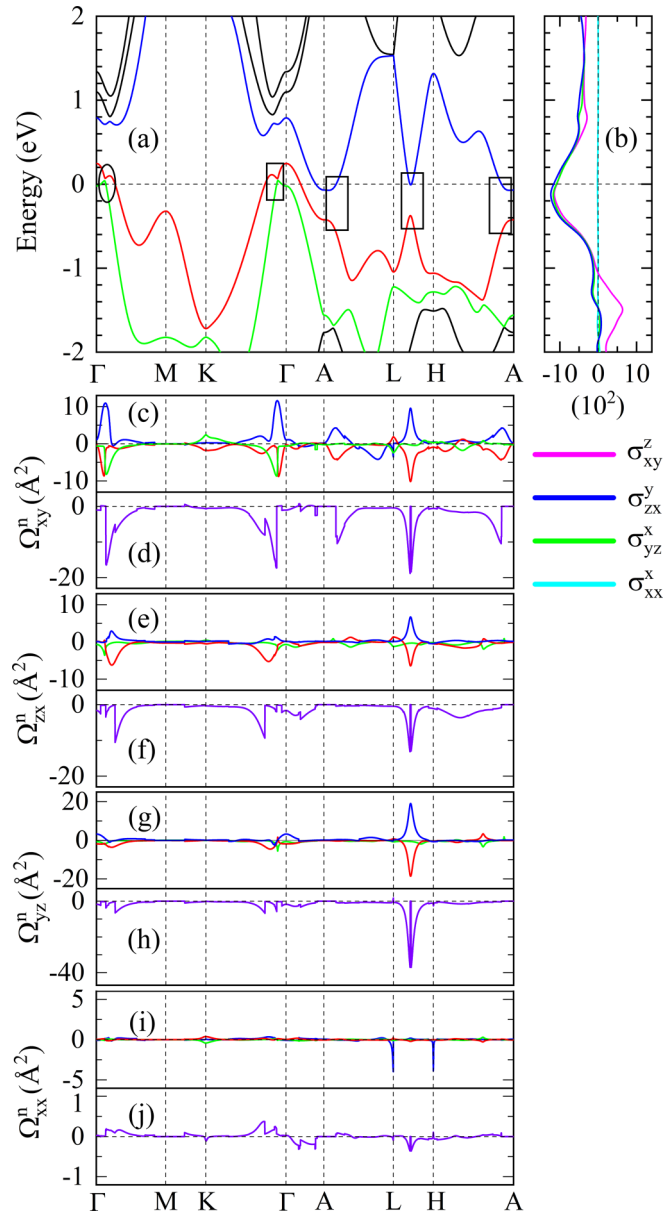

FIG. 3. Bulk Ta_2C. (a) Relativistic band structure; (b) spin Hall conductivities (SHC; σ^z_{xy}, σ^y_{zx}, σ^x_{yz}, and σ^x_{xx}) as a function of energy; (c), (e), (g), (i) band-decomposed spin Berry curvatures (SBC, Ω^n), as well as (d), (f), (h), (j) total SBC along the high-symmetry lines in the Brillouin zone. In (a), (b), the E_F is at zero energy, and the unit of SHC is $10^2\,(\hbar/e)(\Omega\,\mathrm{cm})^{-1}$. In (c)–(j), the unit of SBC is Å^2. Note that in (a), (c), (e), (g), (i), the same color curves correspond to the same bands.

When SOC is considered and the SU(2) symmetry is broken, P1, P2, and L1 are fully gapped [see Fig. 3(a)]. Due to the presence of $\mathcal{PT}$ symmetry, each band becomes doubly degenerate. The SOC lifts the degeneracies of all nodal lines in the band structures of Ta_2C. The SOC-induced band gap is about 24 and 360 meV at P1 and P2, and a maximum value of 550 meV at the Γ point along the Γ-A route, which is significantly larger than V_2C (from 8 to 47 meV) and Nb_2C

TABLE III. Symmetry-imposed tensor forms of the SHC tensors for bulk M_2C with the space group of $P\bar{3}m1$ (164). The layer group of few-layered M_2C is $P\bar{3}m1$, which shares the same tensor form with its bulk counterpart.

	$\underline{\sigma_x}$	$\underline{\sigma_y}$	$\underline{\sigma_z}$
Space group $P\bar{3}m1$	$\begin{pmatrix} \sigma^x_{xx} & 0 & 0 \\ 0 & \sigma^x_{yy} & \sigma^x_{yz} \\ 0 & \sigma^x_{zy} & 0 \end{pmatrix}$	$\begin{pmatrix} 0 & \sigma^y_{xy} & \sigma^y_{xz} \\ \sigma^y_{yx} & 0 & 0 \\ \sigma^y_{zx} & 0 & 0 \end{pmatrix}$	$\begin{pmatrix} 0 & \sigma^z_{xy} & 0 \\ \sigma^z_{yx} & 0 & 0 \\ 0 & 0 & 0 \end{pmatrix}$

(from 11 to 142 meV) (see detailed band structures of M_2C systems in Fig. S4 in the SM [43]). This means that Ta has a much stronger SOC than V and Nb. The phenomenon that the nodal lines are fully gapped under SOC also occurs in crystal systems AX_2 (A = Ca, Sr, Ba; X = Si, Ge, Sn) and CaI_2 with the same space group $P\bar{3}m1$ (164) [49,50].

Since strong SOC-induced band anticrossings around the nodal lines can generate large local SBC, it is expected that M_2C systems have strong SHE [21,51]. To evaluate the SHE in M_2C, we first perform symmetry analysis to evaluate the allowed SHC components. As mentioned above, M_2C has a trigonal crystal structure with the space group $P\bar{3}m1$ (164). The corresponding Laue group is $\bar{3}m$, which leads to the constraints $\sigma^x_{xx} = -\sigma^x_{yy} = -\sigma^y_{yx} = -\sigma^y_{xy}$, $\sigma^y_{zx} = -\sigma^x_{zy}$, $\sigma^y_{xz} = -\sigma^x_{yz}$, and $\sigma^z_{xy} = -\sigma^z_{yx}$ [52], while other tensor elements are zero (see Table III). Thus, M_2C has only four nonzero independent elements, namely, the unconventional component σ^x_{xx} and conventional components σ^x_{yz}, σ^y_{zx}, and σ^z_{xy}. The independent SHC components for M_2C (M = V, Nb, Ta) are shown in Table IV. At first glance, three conventional SHC components are nearly isotropic for V_2C, Nb_2C, and Ta_2C, which are much larger than the unconventional SHC component. Taking σ^z_{xy} as an example, the magnitude of SHC values increases rapidly from top to bottom, which is in accordance with the variation of SOC strength from V to Ta. The SHC at E_F reaches $-1082\,(\hbar/e)(\Omega\,\mathrm{cm})^{-1}$ for Ta_2C, which is comparable to recently reported nodal-line systems, such as InBi $\sim 1100\,(\hbar/e)(\Omega\,\mathrm{cm})^{-1}$ [24], $HfH_2 \sim 1100\,(\hbar/e)(\Omega\,\mathrm{cm})^{-1}$ [53], and 5d transition metal β−$W \sim 1255\,(\hbar/e)(\Omega\,\mathrm{cm})^{-1}$ [54]. We also show energy-dependent SHC (σ^z_{xy}) of Ta_2C in Fig. 3(b) (see SHC components for other M_2C compounds in Fig. S6 in the SM [43]). Interestingly, for a wide range of E_F shifting from $E_F-0.32$ eV to $E_F+0.07$ eV, the magnitude of the σ^z_{xy} component for Ta_2C can still stay larger than $10^3\,(\hbar/e)(\Omega\,\mathrm{cm})^{-1}$.

In order to determine the SHA, we have calculated the longitudinal G_C using the Boltzmann transport equations within the constant relaxation time approximation. According to the experimental resistivity values of 40 $\mu\Omega$ cm of Ta_2C [55], we obtain the corresponding room-temperature relaxation time as 25.3 fs. In addition, we assume that the relaxation times for V_2C and Nb_2C are equal to that of Ta_2C (see G_C in Table S2 in SM [43]). The results in Table IV show that the maximum intrinsic SHA of Ta_2C can reach 8.66%, which is comparable to that of Pt (6.8%) [56].

TABLE IV. Intrinsic SHC and SHA for independent tensor elements for bulk M_2C (M = V, Nb, and Ta). The unit of SHC is $(\hbar/e)(\Omega\,\mathrm{cm})^{-1}$.

	σ^x_{xx}	σ^x_{yz}	σ^y_{zx}	σ^z_{xy}	$\lvert\Theta^x_{xx}\rvert(\%)$	$\lvert\Theta^x_{yz}\rvert(\%)$	$\lvert\Theta^y_{zx}\rvert(\%)$	$\lvert\Theta^z_{xy}\rvert(\%)$
V_2C	−1	−372	−401	−349	0.01	2.81	2.75	2.63
Nb_2C	−6	−566	−588	−564	0.03	2.78	2.63	2.77
Ta_2C	−19	−1090	−1165	−1082	0.15	8.72	6.54	8.66

To figure out the origin of large SHC in M_2C, we calculate the band-decomposed SBC and k-resolved SBC at E_F for Ta_2C in Fig. 3, respectively; the SBC analysis of Nb_2C and V_2C are shown in Fig. S7 in the SM [43]. It is noted that the total SBC at k in Figs. 3(d), 3(f), 3(h), and 3(j) is the summation of SBC on all occupied bands at k.

As can be seen from Figs. 2(a) and 3(a), the nodal lines and points including P1, P2, and L1 are fully gapped under the inclusion of SOC. According to previous reports in the literature, if a Dirac point opens a small hybridization gap with the inclusion of SOC at some k point, then the SBC appears as a pair of peaks with opposite signs on upper and lower bands in the vicinity of this k point [19,20]. If both bands are occupied, the opposite sign of SBC at this k point will cancel out. However, when only one band is occupied, e.g., the E_F falls within the gap, then only one peak of SBC would contribute to the SHC. The phenomenon can be seen in Figs. 3(d), 3(f), and 3(h) for gapped Dirac point P2 along the L-H route.

Apart from Dirac point induced SBC peaks, there also exist other peaks along Γ-M, K-Γ, Γ-A, A-L, and H-A in Fig. 3(d) for the Ω^z_{xy}(k) component. The SBC peaks along K-Γ and Γ-A originate from the gapped nodal point and lines corresponding to P1 and L1. On the other hand, the SBC peaks along A-L and H-A originate from the gapped nodal point at high-symmetry point A (see detailed analysis in Figs. S8 and S9 in SM [43]). In addition, From Eq. (1) and previously reported systems such as ZrXY (X=Si, Ge; Y=S, Se, Te) [19], the SBC peak can also occur at other k points apart from the gapped nodal points. By comparing Figs. 3(c) and 3(d) with Fig. 3(a), the strong local SBC peaks along Γ-M originate from the dashed elliptic area in Fig. 3(a) where there is a tiny energy gap (∼35 meV) between the EB_1 and EB_2 bands. In addition, we also give the contour plots of the $\Omega^z_{xy}(k)$ component in three planes, $k_z = 0$, $k_z = 0.5$, and $k_y = 0$, in Fig. S10 in the SM [43], which clearly show that the SBC is mainly contributed by the gapped nodal lines belonging to classes I and III, and three curved nodal lines of class II. Therefore, the giant SHC found in bulk M_2C (M = V, Nb, Ta) is mainly contributed by the symmetry-protected nodal lines.

C. Electronic band structures and SHE in few-layered M_2C

The intimate relationship between SHC and nodal-line structure in bulk M_2C implies that strong SHE can also exist in monolayer or few-layered M_2C. We first study the SHE of monolayer (1L) M_2C. The symmetry analysis shows that the layer group of few-layered M_2C is $P\bar{3}m1$ with the same tensor constraints and independent SHC components as its bulk counterparts. Table V shows the calculated SHC components for monolayer M_2C. At first glance, the dominant SHC component is σ^z_{xy} for these compounds (see the SBC

TABLE V. Intrinsic SHC and SHA for independent tensor elements for monolayer M_2C (M = V, Nb, and Ta). The unit of SHC is $(\hbar/e)(\Omega\,\mathrm{cm})^{-1}$.

	σ^x_{xx}	σ^x_{yz}	σ^y_{zx}	σ^z_{xy}	$\lvert\Theta^x_{xx}\rvert(\%)$	$\lvert\Theta^x_{yz}\rvert(\%)$	$\lvert\Theta^z_{xy}\rvert(\%)$
V_2C-1L	0	3	3	−25	0	0.05	0.42
Nb_2C-1L	0	6	6	−46	0	0.04	0.35
Ta_2C-1L	4	15	14	−187	0.05	0.19	2.38

analysis of all SHC components for Ta_2C in Figs. S11 and S12 in the SM [43]). The SHC (σ^z_{xy}) increases gradually as SOC strength becomes larger from V_2C to Nb_2C and Ta_2C. The maximum SHC of Ta_2C reaches $-191\,(\hbar/e)(\Omega\,\mathrm{cm})^{-1}$ at E_F. In order to determine the SHA for monolayer M_2C, we directly obtain the electron relaxation time and G_C by evaluating the electron-phonon coupling effects (see G_C and calculation details in Table S3 and Fig. S3 in the SM [43]). The electron relaxation time at E_F is 22.2 fs for Ta_2C. Due to similar electron structures and phonon spectra, we assume that the relaxation times for V_2C and Nb_2C are equal to that of Ta_2C. The results in Table V show that the maximum intrinsic SHA can reach 2.38% for Ta_2C.

V_2C, Nb_2C, and Ta_2C share similar geometries and band structures; therefore, we take Ta_2C as an example to study the layer dependence of independent SHC components by enhancing the thickness from monolayer (1L) up to eight layers (8L). The magnitude of SHC components at E_F versus the number of layers is shown in Fig. 4 and listed in Table S4 in the SM [43]. Meanwhile, we also give the energy dependence of independent SHC components of few-layered Ta_2C in Fig. S13 in the SM [43]. At first glance, the absolute value of the σ^z_{xy} component shows a monotonically increasing trend as the layer number goes from 1L to 8L, while the σ^x_{xx} component maintains a small value less than $20\,(\hbar/e)(\Omega\,\mathrm{cm})^{-1}$. The maximum value of the σ^z_{xy} component is $-608\,(\hbar/e)(\Omega\,\mathrm{cm})^{-1}$, which is larger than 2D systems such as 2L $PtSe_2$ ($\sim 27\,(\hbar/e)(\Omega\,\mathrm{cm})^{-1}$ at E_F [31]), 3L $MoTe_2$ ($\sim 200\,(\hbar/e)(\Omega\,\mathrm{cm})^{-1}$ at E_F [28]), and 1L SnTe ($\sim 245\,(\hbar/e)(\Omega\,\mathrm{cm})^{-1}$ at $E_F + 1.09$ eV [57]). Interestingly,

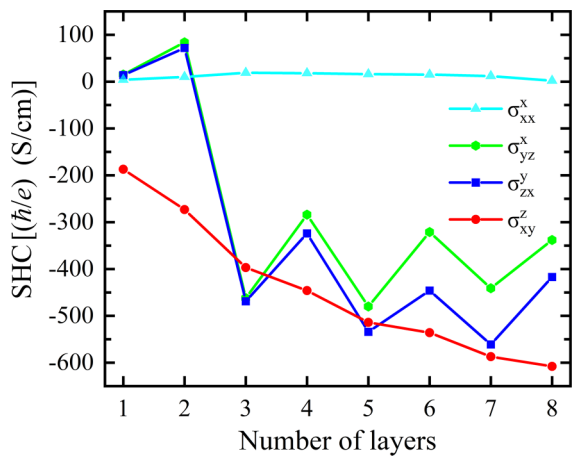

FIG. 4. Layer-dependent SHC components σ^x_{xx}, σ^x_{yz}, σ^y_{zx}, and σ^z_{xy} for 1L-8L Ta_2C.

the magnitude of the σ^x_{yz} and σ^y_{zx} components drops down to $-460\,(\hbar/e)(\Omega\,\mathrm{cm})^{-1}$ at 3L and shows an even-odd oscillation for 4L–8L Ta_2C.

To figure out the origin of layer-dependent SHC observed in few-layered Ta_2C, we take the σ^z_{xy} component as an example to discuss the relationship between the k-resolved SBC and electronic structures for odd-layered Ta_2C in Fig. 5 (see descriptions of even-layered Ta_2C in Figs. S14–S17 in the SM [43]). We note that the magnitude of colors in Figs. 5(m)–5(p) represents the logarithm of the SBC component $\Omega^z_{xy}(k)$ [13]:

$$\text{Magnitude of color bar} = \begin{cases} \mathrm{sgn}\left(\Omega^z_{xy}\right)\log_{10}\left|\Omega^z_{xy}(k)\right| & \left|\Omega^z_{xy}(k)\right| > 10\ \text{Å} \\ \frac{\Omega^z_{xy}(k)}{10} & \left|\Omega^z_{xy}(k)\right| \leqslant 10\ \text{Å} \end{cases}.$$

For band structures without SOC [see Figs. 5(a)–5(d)], we first observe an obvious band crossing between the valence (marked with red lines) and conduction bands along the K-Γ route. As the thickness increases from 1L to 7L Ta_2C, the two bands repeatedly cross each other and induce larger numbers of nodal points, which is protected by $C_{2(110)}$ associated with $\mathcal{PT}$ symmetry (see symmetry analysis in Fig. S18 in the SM [43]). The distribution of nodal points is also given in Figs. 5(e)–5(h). Upon turning on SOC, all the nodal points are fully gapped, resulting in continuous SOC gaps along the Γ-K route. The coexistence of nodal lines and SOC-induced band gaps aligned near the E_F induce large SBC in this system. From Figs. 5(m)–5(p), the magnitude of Ω^z_{xy} becomes larger and denser in the central region of the BZ and the distribution of Ω^z_{xy} extends out along the Γ-K and Γ-M directions, which is in accordance with the variation of distribution of nodal points in the first BZ. In addition, apart from the Γ-K and Γ-M directions, we also find that the distributions of Ω^z_{xy} in Figs. 5(o) and 5(p) extend to the edges of the BZ in other directions. This is because there exist other nodal points induced by band crossing of other pairs of bands near E_F. Therefore, the layer-dependent nodal-point structures play an important role in determining the increasing trend of the Ω^z_{xy} component. Apart from the Ω^z_{xy} component, we also give Ω^y_{zx}, Ω^x_{yz}, and Ω^x_{xx} components for odd- and even-layered Ta_2C in Figs. S14–S17 in the SM [43]. As the layer thickness increases in odd numbers, the increasing trend of the Ω^y_{zx} and Ω^x_{yz} components in the first BZ is similar to that of the Ω^z_{xy} component. However, the appearance of SBC regions with opposite sign for adjacent even-layered Ta_2C induces the decline of net SBC at E_F and even-odd oscillation for σ^x_{yz} and σ^y_{zx} SHC components.

IV. DISCUSSION AND CONCLUSIONS

We take M_2C (M = V, Nb, and Ta) as a representative in the above presentation. As shown in Fig. S19 in the SM [43], the essential band crossings between the bands near the E_F are also shared by other members of the MXenes. In most materials, like Zr_2C, Hf_2C, Nb_2N, and Ta_2N, the band crossing points are below or above the E_F, while in other materials such as Zr_2N and Hf_2N, the band crossing points are just at the E_F; these are expected to give rise to strong SHC.

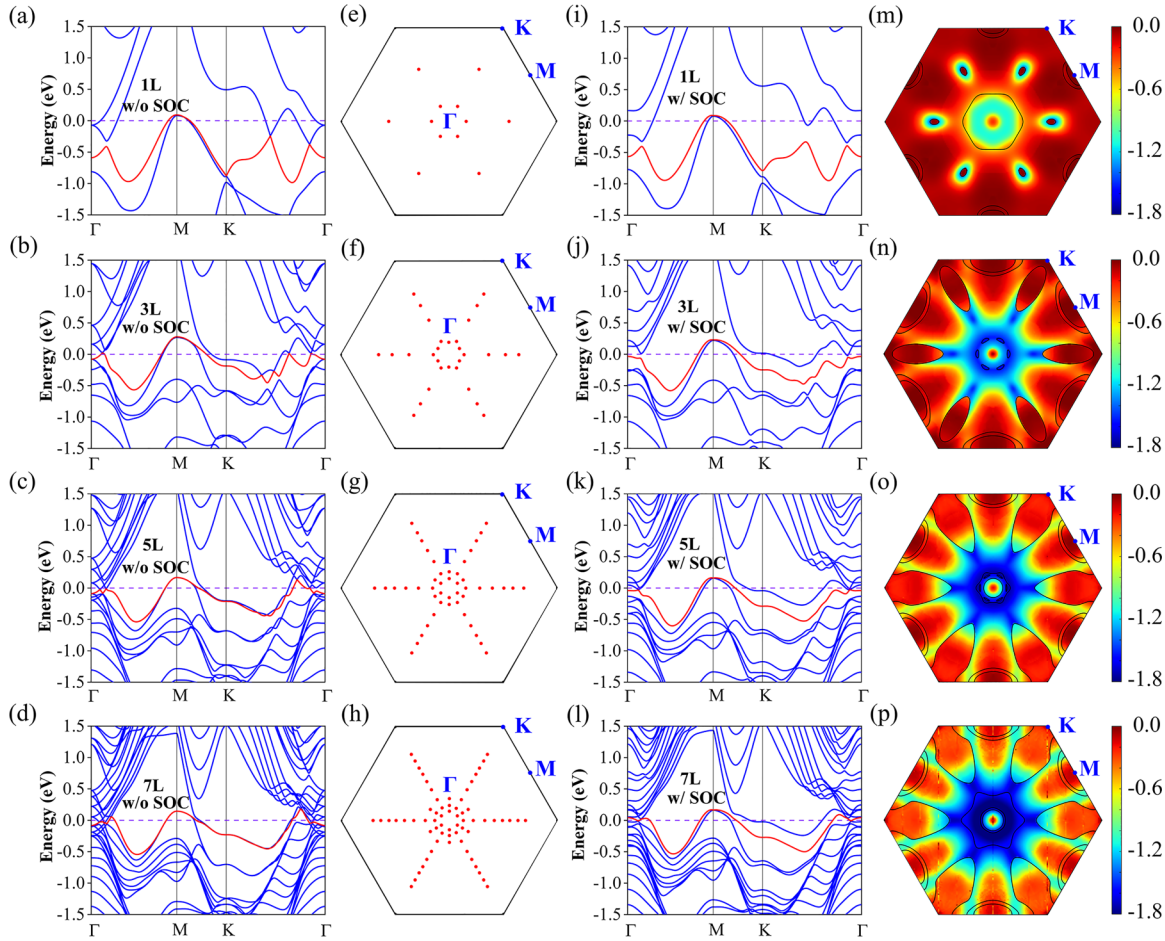

FIG. 5. (a)–(d) Band structures for 1L, 3L, 5L, and 7L Ta_2C without SOC, respectively. (e)–(h) Corresponding nodal-point structures in the first BZ. (i)–(l) Band structures for 1L, 3L, 5L, and 7L monolayer Ta_2C with SOC, respectively. (m)–(p) Corresponding σ_{xy}^{z} component of SBC in first BZ. Note that the high-symmetry points are denoted as blue dots in (e)–(h) and (m)–(p).

Apart from controlling SHE by layer thickness, we also study the stacking-dependent SHE in bilayer layer Ta_2C with AA and AB stacking modes (see Fig. S20 in the SM [43]). The results show that the magnitude of the SHC components σ_{yz}^{x}, σ_{zx}^{y}, and σ_{xy}^{z} at E_F increases obviously by changing AA to AB stacking configurations.

In summary, we have predicted large intrinsic SHE in layered transition metal carbides M_2C (M = V, Nb, and Ta). Due to strong SOC and contributions of multiple nodal lines in the band structure, the SHC and SHA of bulk Ta_2C can reach up to $\sim 1100\,(\hbar/e)(\Omega\,\mathrm{cm})^{-1}$ and $\sim 8.66\%$, respectively. For few-layered Ta_2C, the σ_{xy}^{z} component of SHC exhibits a monotonic increase as the number of layers increases, while σ_{yz}^{x} and σ_{zx}^{y} components show an even-odd oscillation for 3L–8L. The maximum value of SHC is $-608\,(\hbar/e)(\Omega\,\mathrm{cm})^{-1}$ for 8L Ta_2C, which is larger than many 2D systems reported so far and comparable to many 3D topological systems. Therefore, one can effectively tune the SHC by controlling the layer thickness in layered 2D materials. Our results not only elucidate the interplay between layer-dependent SHC and band topology, but also provide theoretical guidance for developing next-generation spintronic devices.

ACKNOWLEDGMENTS

This work is supported by the National Natural Science Foundation of China (Grants No. 12304139, No. 12074111, and No. 52272108), the Natural Science Foundation of Hubei Province (Grants No. 2023AFB434 and No. 2023AFA105), and the Natural Science Foundation of Shandong Province (Grants No. ZR2020MA068 and No. ZR2023MA018).

[1] M. I. D'yakonov and V. I. Perel', Spin orientation of electrons associated with the interband absorption of light in semiconductors, Zh. Eksp. Teor. Fiz. **60**, 1954 (1971) [Sov. Phys. JETP **33**, 1053 (1971)].

[2] J. E. Hirsch, Spin Hall effect, Phys. Rev. Lett. **83**, 1834 (1999).

[3] S. Murakami, N. Nagaosa, and S.-C. Zhang, Dissipationless quantum spin current at room temperature, Science **301**, 1348 (2003).

[4] J. Sinova, D. Culcer, Q. Niu, N. A. Sinitsyn, T. Jungwirth, and A. H. MacDonald, Universal intrinsic spin Hall effect, Phys. Rev. Lett. **92**, 126603 (2004).

[5] Y. K. Kato, R. C. Myers, A. C. Gossard, and D. D. Awschalom, Observation of the spin Hall effect in semiconductors, Science **306**, 1910 (2004).

[6] S. O. Valenzuela and M. Tinkham, Direct electronic measurement of the spin Hall effect, Nature (London) **442**, 176 (2006).

[7] J. Sinova, S. O. Valenzuela, J. Wunderlich, C. H. Back, and T. Jungwirth, Spin Hall effects, Rev. Mod. Phys. **87**, 1213 (2015).

[8] N. Okuma and M. Ogata, Unconventional spin Hall effect and axial current generation in a Dirac semimetal, Phys. Rev. B **93**, 140205(R) (2016).

[9] B. B. Prasad and G.-Y. Guo, Tunable spin Hall and spin Nernst effects in Dirac line-node semimetals XCuYAs (X = Zr, Hf; Y = Si, Ge), Phys. Rev. Mater. **4**, 124205 (2020).

[10] K. Tang, Y.-C. Lau, K. Nawa, Z. Wen, Q. Xiang, H. Sukegawa, T. Seki, Y. Miura, K. Takanashi, and S. Mitani, Spin Hall effect in a spin-1 chiral semimetal, Phys. Rev. Res. **3**, 033101 (2021).

[11] T.-Y. Hsieh, B. B. Prasad, and G.-Y. Guo, Helicity-tunable spin Hall and spin Nernst effects in unconventional chiral fermion semimetals XY (X = Co, Rh; Y = Si, Ge), Phys. Rev. B **106**, 165102 (2022).

[12] G. Y. Guo, S. Murakami, T.-W. Chen, and N. Nagaosa, Intrinsic spin Hall effect in platinum: First-principles calculations, Phys. Rev. Lett. **100**, 096401 (2008).

[13] J. Qiao, J. Zhou, Z. Yuan, and W. Zhao, Calculation of intrinsic spin Hall conductivity by Wannier interpolation, Phys. Rev. B **98**, 214402 (2018).

[14] N. H. D. Khang, Y. Ueda, and P. N. Hai, A conductive topological insulator with large spin Hall effect for ultralow power spin-orbit torque switching, Nat. Mater. **17**, 808 (2018).

[15] D.-F. Shao, G. Gurung, S.-H. Zhang, and E. Y. Tsymbal, Dirac nodal line metal for topological antiferromagnetic spintronics, Phys. Rev. Lett. **122**, 077203 (2019).

[16] K. Kondou, H. Chen, T. Tomita, M. Ikhlas, T. Higo, A. H. MacDonald, S. Nakatsuji, and Y. Otani, Giant field-like torque by the out-of-plane magnetic spin Hall effect in a topological antiferromagnet, Nat. Commun. **12**, 6491 (2021).

[17] Y. Fan *et al.*, Magnetization switching through giant spin-orbit torque in a magnetically doped topological insulator heterostructure, Nat. Mater. **13**, 699 (2014).

[18] Y. Wang, P. Deorani, K. Banerjee, N. Koirala, M. Brahlek, S. Oh, and H. Yang, Topological surface states originated spin-orbit torques in Bi_2Se_3, Phys. Rev. Lett. **114**, 257202 (2015).

[19] Y. Yen and G.-Y. Guo, Tunable large spin Hall and spin Nernst effects in the Dirac semimetals ZrXY (X = Si, Ge; Y = S, Se, Te), Phys. Rev. B **101**, 064430 (2020).

[20] Y. Sun, Y. Zhang, C. Felser, and B. Yan, Strong intrinsic spin Hall effect in the TaAs family of Weyl semimetals, Phys. Rev. Lett. **117**, 146403 (2016).

[21] Y. Sun, Y. Zhang, C.-X. Liu, C. Felser, and B. Yan, Dirac nodal lines and induced spin Hall effect in metallic rutile oxides, Phys. Rev. B **95**, 235104 (2017).

[22] E. Derunova, Y. Sun, C. Felser, S. S. P. Parkin, B. Yan, and M. N. Ali, Giant intrinsic spin Hall effect in W_3Ta and other A15 superconductors, Sci. Adv. **5**, eaav8575 (2019).

[23] W. Hou, J. Liu, X. Zuo, J. Xu, X. Zhang, D. Liu, M. Zhao, Z.-G. Zhu, H.-G. Luo, and W. Zhao, Prediction of crossing nodal-lines and large intrinsic spin Hall conductivity in topological Dirac semimetal Ta_3As family, npj Comput. Mater. **7**, 37 (2021).

[24] Y. Zhang, Q. Xu, K. Koepernik, C. Fu, J. Gooth, J. van den Brink, C. Felser, and Y. Sun, Spin Nernst effect in a p-band semimetal InBi, New J. Phys. **22**, 093003 (2020).

[25] G. M. Stiehl, R. Li, V. Gupta, I. El Baggari, S. Jiang, H. Xie, L. F. Kourkoutis, K. F. Mak, J. Shan, R. A. Buhrman *et al.*, Layer-dependent spin-orbit torques generated by the centrosymmetric transition metal dichalcogenide β-$MoTe_2$, Phys. Rev. B **100**, 184402 (2019).

[26] Q. Shao, G. Yu, Y.-W. Lan, Y. Shi, M.-Y. Li, C. Zheng, X. Zhu, L.-J. Li, P. K. Amiri, and K. L. Wang, Strong Rashba-Edelstein effect-induced spin-orbit torques in monolayer transition metal dichalcogenide/ferromagnet bilayers, Nano Lett. **16**, 7514 (2016).

[27] G. M. Stiehl, D. MacNeill, N. Sivadas, I. El Baggari, M. H. D. Guimarães, N. D. Reynolds, L. F. Kourkoutis, C. J. Fennie, R. A. Buhrman, and D. C. Ralph, Current-induced torques with Dresselhaus symmetry due to resistance anisotropy in 2D materials, ACS Nano **13**, 2599 (2019).

[28] P. Song, C.-H. Hsu, G. Vignale, M. Zhao, J. W. Liu, Y. J. Deng, W. Fu, Y. P. Liu, Y. B. Zhang, H. Lin, V. M. Pereira, and K. P. Loh, Coexistence of large conventional and planar spin Hall effect with long spin diffusion length in a low-symmetry semimetal at room temperature, Nat. Mater. **19**, 292 (2020).

[29] B. Zhao, D. Khokhriakov, Y. Zhang, H. Fu, B. Karpiak, A. Md. Hoque, X. Xu, Y. Jiang, B. Yan, and S. P. Dash, Observation of charge to spin conversion in Weyl semimetal WTe_2 at room temperature, Phys. Rev. Res. **2**, 013286 (2020).

[30] H. Xu, J. Wei, H. Zhou, J. Feng, T. Xu, H. Du, C. He, J. Zhang, Y. Huang, Y. Liu, H.-C. Wu, C. Guo, X. Wang, Y. Guang, H. Wei, Y. Peng, W. Jiang, G. Yu, and X. Han, High spin Hall conductivity in large-area type-II Dirac semimetal $PtTe_2$, Adv. Mater. **32**, 2000513 (2020).

[31] J. Li, H. Jin, Y. Wei, and H. Guo, Tunable intrinsic spin Hall conductivity in bilayer $PtTe_2$ by controlling the stacking mode, Phys. Rev. B **103**, 125403 (2021).

[32] Y. Gogotsi and B. Anasori, The rise of MXenes, ACS Nano **13**, 8491 (2019).

[33] M. Naguib, M. W. Barsoum, and Y. Gogotsi, Ten years of progress in the synthesis and development of MXenes, Adv. Mater. **33**, 2103393 (2021).

[34] G. Gao, G. Ding, J. Li, K. Yao, M. Wu, and M. Qian, Monolayer MXenes: Promising half-metals and spin gapless semiconductors, Nanoscale **8**, 8986 (2016).

[35] A. Sufyan, A. B. Maghirang, G. Macam, Z.-Q. Huang, C.-H. Hsu, and F.-C. Chuang, Electronic and topological band evolution of VB-group transition metal monocarbides M_2C (M = V, Nb, or Ta) bulk and monolayer, Mater. Today Commun. **32**, 103875 (2022).

[36] Y. Luo, C. Cheng, H.-J. Chen, K. Liu, and X.-L. Zhou, Systematic investigations of the electron, phonon and elastic properties of monolayer M_2C (M = V, Nb, Ta) by first-principles calculations, J. Phys.: Condens. Matter **31**, 405703 (2019).

[37] N. J. Lane, M. W. Barsoum, and J. M. Rondinelli, Correlation effects and spin-orbit interactions in two-dimensional hexagonal $5d$ transition metal carbides, $Ta_{n+1}C_n$ (n = 1, 2, 3), Europhys. Lett. **101**, 57004 (2013).

[38] P. Giannozzi, S. Baroni, N. Bonini, M. Calandra, R. Car, C. Cavazzoni, D. Ceresoli, G. L. Chiarotti, M. Cococcioni, I. Dabo, A. Dal Corso, S. Fabris, G. Fratesi, S. de Gironcoli, R. Gebauer, U. Gerstmann, C. Gougoussis, A. Kokalj, M. Lazzeri,

L. Martin-Samos *et al.*, QUANTUM ESPRESSO: A modular and open-source software project for quantum simulations of materials, J. Phys.: Condens. Matter **21**, 395502 (2009).

[39] P. E. Blöchl, Projector augmented-wave method, Phys. Rev. B **50**, 17953 (1994).

[40] J. P. Perdew, K. Burke, and M. Ernzerhof, Generalized gradient approximation made simple, Phys. Rev. Lett. **77**, 3865 (1996).

[41] N. Marzari, A. A. Mostofi, J. R. Yates, I. Souza, and D. Vanderbilt, Maximally localized Wannier functions: Theory and applications, Rev. Mod. Phys. **84**, 1419 (2012).

[42] A. A. Mostofi, An updated version of WANNIER90: A tool for obtaining maximally-localised Wannier functions, Comput. Phys. Commun. **185**, 2309 (2014).

[43] See Supplemental Material at http://link.aps.org/supplemental/10.1103/PhysRevB.108.195129 for additional DFT results.

[44] Q. Wu, S. Zhang, H.-F. Song, M. Troyer, and A. A. Soluyanov, WANNIERTOOLS: An open-source software package for novel topological materials, Comput. Phys. Commun. **224**, 405 (2018).

[45] G. Pizzi, BOLTZWANN: A code for the evaluation of thermoelectric and electronic transport properties with a maximally-localized Wannier functions basis, Comput. Phys. Commun. **185**, 422 (2014).

[46] S. Poncé, E. R. Margine, C. Verdi, and F. Giustino, EPW: Electron–phonon coupling, transport and superconducting properties using maximally localized Wannier functions, Comput. Phys. Commun. **209**, 116 (2016).

[47] A. L. Bowman, T. C. Wallace, J. L. Yarnell, R. Wenzel, and E. K. Storms, The crystal structures of V_2C and Ta_2C, Acta Cryst. **19**, 6 (1965).

[48] G. Brauer, H. Renner, and J. Wernet, Die carbide des niobs, Z. Anorg. Allg. Chem. **277**, 249 (1954).

[49] H. Huang, J. Liu, D. Vanderbilt, and W. Duan, Topological nodal-line semimetals in alkaline-earth stannides, germanides, and silicides, Phys. Rev. B **93**, 201114(R) (2016).

[50] M.-X. Wu, D.-S. Ma, Tie Yang, Y.-H. Wei, K. Chai, P. Wang, B. Wang, and M.-Q. Kuang, Straight and twisted open nodal-line phonon states in the CaI_2 family of materials, Phys. Chem. Chem. Phys. **25**, 10561 (2023).

[51] N.-N. Zhao, K. Liu, and Z.-Y. Lu, Large intrinsic spin Hall conductivity and spin Hall angle in the nodal-line semimetals $ThAl_2$ and $ThGa_2$, Phys. Rev. B **105**, 235119 (2022).

[52] A. Roy, M. H. D. Guimarães, and J. Sławińska, Unconventional spin Hall effects in nonmagnetic solids, Phys. Rev. Mater. **6**, 045004 (2022).

[53] X. Zuo, Q. Gao, X. Sui, X. Xu, X. Jiang, L. Han, H. Li, D. Li, D. Liu, B. Huang, and B. Cui, Giant and robust intrinsic spin Hall effects in metal dihydrides: A first-principles prediction, Phys. Rev. B **103**, 125159 (2021).

[54] X. Sui, C. Wang, J. Kim, J. Wang, S. H. Rhim, W. Duan, and N. Kioussis, Giant enhancement of the intrinsic spin Hall conductivity in β-tungsten via substitutional doping, Phys. Rev. B **96**, 241105(R) (2017).

[55] R. Steinitz and R. Resnick, Electrical and magnetic properties of compositions in the tantalum-carbon system, J. Appl. Phys. **37**, 3463 (1966).

[56] Y. Wang, P. Deorani, X. Qiu, J. H. Kwon, and H. Yang, Determination of intrinsic spin Hall angle in Pt, Appl. Phys. Lett. **105**, 152412 (2014).

[57] J. Sławińska, F. T. Cerasoli, H. Wang, S. Postorino, A. Supka, S. Curtarolo, M. Fornari, and M. Buongiorno Nardelli, Giant spin Hall effect in two-dimensional monochalcogenides, 2D Mater. **6**, 025012 (2019).